Materials Horizons

ROYAL SOCIETY OF CHEMISTRY

COMMUNICATION

View Article Online
View Journal | View Issue

Check for updates

Cite this: *Mater. Horiz.*, 2022, 9, 1921

Received 6th March 2022,
Accepted 25th April 2022

DOI: 10.1039/d2mh00284a

rsc.li/materials-horizons

Hydrogel- and organohydrogel-based stretchable, ultrasensitive, transparent, room-temperature and real-time NO_2 sensors and the mechanism†

Yaoming Wei,‡[a] Hao Wang,‡[a] Qiongling Ding,[a] Zixuan Wu,[a] He Zhang,[b] Kai Tao,[c] Xi Xie[a] and Jin Wu*[a]

Highly stretchable, sensitive and room-temperature nitrogen dioxide (NO_2) sensors are fabricated by exploiting intrinsically stretchable, transparent and ion-conducting hydrogels and active metals as the novel transducing materials and electrodes, respectively. The NO_2 sensor exhibits high sensitivity (60.02% ppm^{-1}), ultralow theoretical limit of detection (6.8 ppb), excellent selectivity, linearity and reversibility at room temperature. Notably, the sensitivity can be maintained even under 50% tensile strain. For the first time, it's found that the metal electrodes significantly impact the sensing performance. Specifically, the sensitivity is boosted from 31.18 to 60.02% ppm^{-1} by replacing the anodic silver with copper–tin alloy. Importantly, by applying specially designed sensing tests, and microscopic and composition analyses, we have obtained the inherent NO_2 sensing mechanism: the anodic metal tends to be oxidized and the NO_2 molecules tend to react in the cathode–gel interface. The introduction of glycerol converts the hydrogel into the organohydrogel with remarkably enhanced anti-drying and anti-freezing capacities and toughness, which effectively improved the long-time stability of the sensors. Importantly, we execute sound/light alarms and a wireless smartphone alarm by utilizing a designed circuit board and applet. This work gives an incisive investigation for the preparation, performance improvement, mechanism and application of hydrogel-based NO_2 sensors, promoting the evolution of hydrogel ionotronics.

New concepts

The conventional sensing materials (*e.g.*, oxide semiconductors) for gas sensors struggle to meet the growing requirement of wearable and flexible electronics on account of the lack of stretchability and transparency, and the demand for high temperature to promote the sensing process, leading to accessorial power dissipation and complicated fabrication processes. Herein, we employ ion-conductive hydrogels and metals as the electrolytes and electrodes, respectively, to fabricate intrinsically stretchable, transparent, and room-temperature NO_2 sensors with impressive performance. This sensor is able to maintain its sensing capability while withstanding drastic deformations (*e.g.*, 50% strain). Importantly, for the first time, we find the dependency relationship between the electrodes and sensing performances of hydrogels by exploring and analysing the sensing behaviours with different anodes, based on which, the sensing performance is boosted by modifying the electrodes. The response mechanism is revealed as well: NO_2 molecules tend to react in the cathode while the anodic metal tends to be oxidized. Importantly, we also execute a wireless gas alarm in a smartphone and a sound/light alarm by collecting and processing the real-time signals from the sensors. This work will remarkably promote the development of stretchable and flexible gas sensors by exploiting ion-conductive hydrogels and organohydrogels as novel transducing materials.

1. Introduction

Portable and wearable electronic devices have attracted increasing research interest due to the rapid evolution and urgent demands in healthcare monitoring, consumer electronics and internet of things (IoT).[1–3] Different from the traditional rigid electronic devices, stretchable devices can adapt to various irregular surfaces and deformations so as to endow the devices with good compliance and wearing comfort. More impressively, stretchable devices attached to the human skin are able to be used as wearable sensors to monitor various physiological and environmental signals continuously and expediently, such as human motions, body temperature and other vital signs, environmental humidity, vapors, *etc.*[4,5] Among these sensing devices, gas sensors are significant for environment/healthcare monitoring, safety, early warning, *etc.* For instance, excessive sulfur dioxide (SO_2) and

---

[a] *State Key Laboratory of Optoelectronic Materials and Technologies and the Guangdong Province Key Laboratory of Display Material and Technology, School of Electronics and Information Technology, Sun Yat-sen University, Guangzhou 510275, China. E-mail: wujin8@mail.sysu.edu.cn*

[b] *National Engineering Research Center of Novel Equipment for Polymer Processing, Key Laboratory of Polymer Processing Engineering (SCUT), Ministry of Education, South China University of Technology, Guangzhou, 510641, China*

[c] *Ministry of Education Key Laboratory of Micro and Nano Systems for Aerospace, Northwestern Polytechnical University, Xi'an 710072, China*

† Electronic supplementary information (ESI) available: Supporting Information and Supporting Movies are available from the RSC Online or from the author. See DOI: https://doi.org/10.1039/d2mh00284a

‡ Yaoming Wei and Hao Wang contributed equally to this work.

nitrogen dioxide (NO_2) in the atmosphere will provoke acid rain, endangering the natural ecology and human health. The precise detection of trace-level NO_2 is also vital since NO_2 at low concentration could harm the respiratory system of humans.[6,7]

In past decades, multitudinous sensing materials have been explored and applied to fabricate gas sensors with superior sensitivities, *e.g.*, metal oxide semiconductors, carbon nanotubes and some burgeoning two-dimensional materials.[7–12] Nevertheless, most of them are rigid, opaque and lack deformability, making them not advisable in wearable applications.[13] Furthermore, the operation of metal oxide-based gas sensors generally requires the presence of oxygen. Although integrating the rigid sensing materials into flexible substrates (*e.g.*, polydimethylsiloxane, polyimide and Ecoflex) enables sensors to operate under some deformations, the strain range is usually narrow (less than 100% tensile strain).[14,15] Furthermore, the commercially available metal oxide semiconductors usually require a high-temperature operating condition, resulting in complicated device fabrication, increased power consumption and thermal safety issues in wearable applications. In addition, to achieve application in wearable devices, the transparency of the sensor should be taken into account. A high transparency not only reduces the optic differences between human skin and wearable devices to improve the aesthetics effect, but enables the visualization of the internal structure below the electronics without impeding the function of the device.[16] In particular, for flexible touch panels, a good transparency is necessary for transmitting light information.[17] Hence, developing intrinsically stretchable and transparent gas sensing materials with excellent performance at room temperature becomes crucial and urgent.

Hydrogel is composed of a three-dimensional polymeric network swelled in water, which combines solid-like appearance, stretchability and elasticity with liquid-like ionic transporting behaviour. Moreover, some hydrogels uniquely exhibit attractive self-healability and high transparency, which is beneficial for cyclic, sustainable applications and aesthetic design.[18–21] Among all kinds of hydrogels, ionically and covalently crosslinked double-network (DN) hydrogels have attracted tremendous research interest due to their fascinating mechanical toughness, high stretchability and electrical properties.[22–25] In these cases, the monomers crosslink to form the first covalently crosslinked network with the aid of crosslinkers while some chains of molecules crosslink to form a second ionically crosslinked network with the assistance of specific ions, leading to enhanced toughness and stretchability.[26] Furthermore, ion-conducting hydrogels can electrically respond to various stimuli such as temperature, humidity, ion, strain and pressure, *etc.*, showing great application potential in wearable electronics.[27–33]

At present, concentrated endeavor has been devoted to constructing hydrogel-based flexible strain/pressure sensors for real-time monitoring of human motion and biological signals, but the research on ion-conducting hydrogel-based stretchable NO_2 gas sensors is relatively infrequent.[34–37] Wu *et al.* first reported a stretchable polyacrylamide (PAM)/carrageenan DN hydrogel-based NO_2 sensor with an air background.[34,35] This sensor showed a sensitivity of 33.2% ppm^{-1} to NO_2.[34] Zhi *et al.* attributed the NO_2 and NH_3 gas responsive behaviors of the hydrogels to hydrogen bonds, molecule crystallization, and electrostatic interactions inside the hydrogels.[36] Liu and the co-workers reported a hydrogel film-based ammonia (NH_3) sensor, which employed an alternating current power supply and showed a high response of 6.2 (Z_a/Z_g) to 20 ppm NH_3 due to the reaction between the carboxyl group of the hydrogel and NH_3 leading to changes in ionic conduction.[37] By contrast, the response of their hydrogel film to NO_2 is extremely low. Theoretically, the ion-conductive hydrogels function like an electrolyte while connected with a direct-current (DC) power supply using electrodes. Therefore, the redox reactions of oxidizing NO_2 gas and charge transfer process at electrodes will critically influence the current in the circuit if a DC power supply is employed, bringing about gas responsive behaviours. However, existing works failed to realize the significance of redox reactions that occurred at the electrode–hydrogel interfaces, and therefore the precise sensing mechanism is still unclear. Furthermore, the important role of the electrode in the gas sensing properties of ion-conductive hydrogels has not yet been explored. In addition, an integrated hydrogel-based NO_2 sensor for sound/light alarms and a wireless smartphone alarm has not yet been developed. Last but not least, tough hydrogel (*e.g.* PAM/calcium alginate (CA))-based stretchable NO_2 sensors have seldom been reported.

Despite the intriguing advantages of hydrogels in fabricating intrinsically stretchable electronics, the changes in temperature or humidity (especially the high temperature and low humidity) have remarkably detrimental influences on the properties and sensing behaviours of hydrogels, and the resulting inferior stability of hydrogel-based sensors seriously impedes their practical applications. For example, as time goes by, the mechanical and electrical properties of hydrogels will degenerate because of the severe water loss. As we all know, it is indispensable to directly expose hydrogel-based gas and humidity sensors to the surrounding environment for the detection of chemical stimuli, and this will further aggravate the dehydration of hydrogels. Furthermore, the freezing of water in hydrogels at subzero temperatures deprives the flexibility, stretchability, transparency and sensing function of hydrogels simultaneously. Therefore, boosting the moisture retention and anti-freezing capacities to achieve a superior stability is exigent for hydrogel-based electrical devices to broaden their application scope. To this end, introducing moisture absorbents into hydrogels to improve their moisture retention capacity is proven as an efficient method.[30,35,38,39] Specific salts (such as potassium chloride (KCl) and calcium chloride ($CaCl_2$)) incorporated in the hydrogels endow them with better moisture retention capacity compared with the unmodified counterparts. It is found that the water–polyol binary solvent can enhance the long-term stability of hydrogel-based devices obviously because of the formation of abundant hydrogen bonds between water and polyol molecules.[30,38–40] The impact of polyols such as glycerol (Gly) on the gas sensing properties (*e.g.* stability, sensitivity) of the hydrogel/organohydrogel is investigated in this work.

Herein, for the first time, we utilized the intrinsically stretchable, transparent, tough and ion-conducting PAM/CA

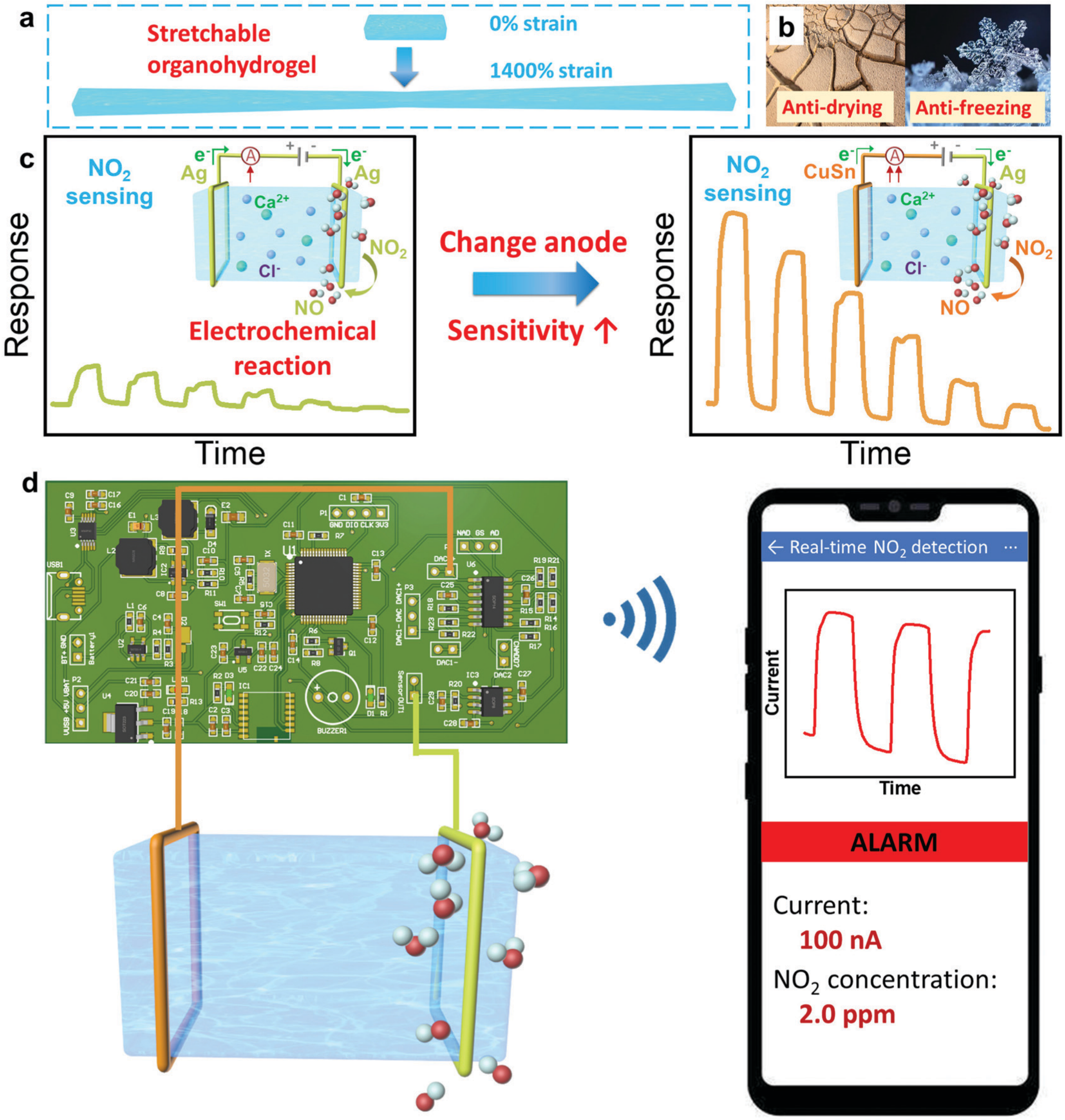

Fig. 1 Schematics illustrating (a) the high stretchability of the hydrogel, and (b) the anti-drying and anti-freezing capacities of the organohydrogels, respectively. (c) The electrode-dependent NO_2 sensing performance and sensing mechanism of the hydrogel sensors. (d) The wireless alarm demonstration of the hydrogel-based NO_2 sensor by a circuit board and an applet in a smartphone.

DN hydrogel/organohydrogel equipped with metal electrodes to fabricate stretchable gas sensors. The hydrogel is able to withstand 1400% tensile strain due to its unique DN structure (Fig. 1(a)). Gly was introduced in the solvent of the hydrogel, which converts hydrogels into tough organohydrogels with boosted long-term stability (anti-drying and anti-freezing abilities), leading to better durability and broader application environmental conditions of the gas sensors (Fig. 1(b)). Interestingly, it is found that the gas sensing performances of hydrogels can be boosted by tailoring the composition of the electrodes (Fig. 1(c)). Specifically, the sensitivity is improved from 31.18 to as high as 60.02% ppm^{-1} at room temperature by employing copper–tin (CuSn) alloy to replace the silver (Ag) anode material, demonstrating the important role of the electrode in the gas sensing of hydrogels. To understand the in-depth sensing mechanism, microscopic analyses of metal electrodes are conducted before and after gas sensing tests. It is found that NO_2 molecules tend to diffuse and adsorb in the cathode and participate in the electrode reactions, promoting the charge transfer process and increasing the current in the circuit (Fig. 1(c)). Importantly, the gas sensors are capable of working normally under drastic mechanical deformations (*e.g.* 50% stretching strain) and in an anaerobic environment, favouring wearable application development. Furthermore, we also demonstrate sound and light alarms of real-time NO_2 detection *via* well-designed circuit boards and a wireless smartphone, which brings the convenience of early warning in practical applications (Fig. 1(d)).

2. Results and discussion

2.1 Synthesis and characterization of hydrogels and organohydrogels

Different from the traditional one-step method, here we developed a facile, two-step strategy to prepare the PAM/CA-based DN tough hydrogels (Fig. 2(a)). Concretely speaking, the covalently crosslinked PAM network was initially formed from acrylamide (AM) monomers with the assistance of a crosslinker in the first step. Subsequently, another ionically crosslinked CA network was converted from sodium alginate (SA) through the introduction of Ca^{2+} *via* a facile soaking and salt infiltration process (Experimental section and Fig. 2(b)). As a result, the DN hydrogel consisting of PAM and CA dual networks was successfully constructed. With this method, the conductivity and mechanical properties of the hydrogel can be adjusted conveniently by changing the concentration and soaking time of the $CaCl_2$ solution.

Benefiting from the complementary nature of these two polymer networks, this unique DN structure endows the hydrogel with outstanding mechanical properties. When the DN hydrogel withstands adscititious deformations, the CA network can be unlocked to dissipate energy efficiently and thus prevent the hydrogel from being destroyed. Meanwhile, the combination of the crack bridging effect and the background hysteresis effect provided by the covalently crosslinked PAM and

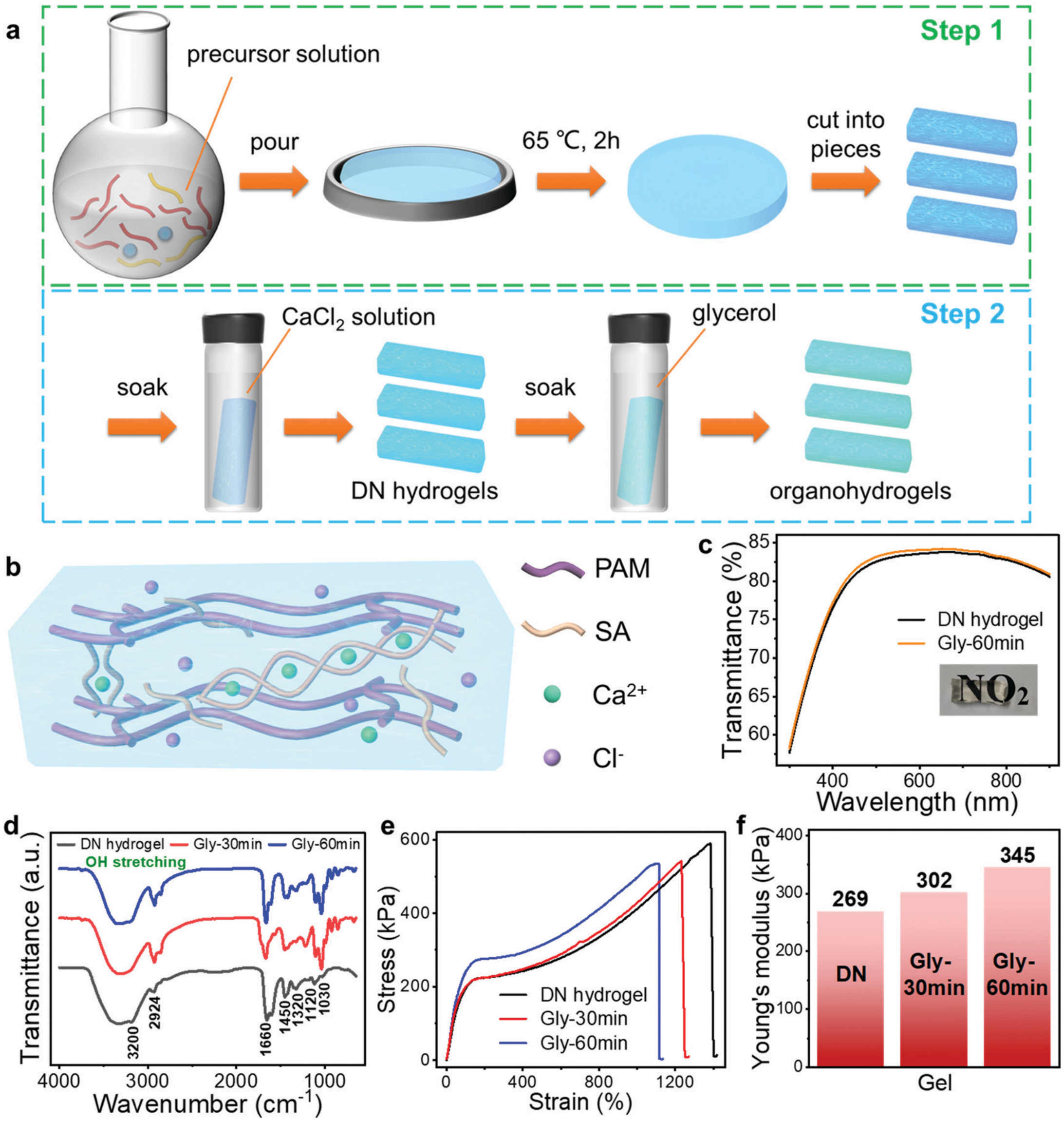

Fig. 2 (a) Schematic illustrating the two-step synthesis process of the DN hydrogels and organohydrogels. (b) Schematic showing the DN structure of the ion-conducting PAM/CA hydrogel. (c) The transmittance spectra of the DN hydrogel and organohydrogel. Inset shows that the word "NO_2" on paper can be clearly seen through a small piece of hydrogel, suggesting high transparency. (d) FTIR spectra of the DN hydrogel and organohydrogels. (e) The curves of tensile stress *versus* strain of the DN hydrogel and organohydrogels. (f) The Young's moduli of the DN hydrogel and organohydrogels acquired from the linear regions of the curves in (e).

ionically crosslinked CA networks, respectively, contributes to the high toughness of the DN hydrogel.[41] Therefore, it is feasible for the DN hydrogel-based sensor to operate in a highly deformed state, enhancing the robustness enormously. To further strengthen the environmental stability and mechanical toughness, the organohydrogels are obtained through a solvent replacement strategy, in which the water of hydrogels is partially replaced with Gly by soaking the as-prepared hydrogels in Gly for tens of minutes (Fig. 2(a) and Experimental section). Satisfactorily, both the DN hydrogel and organohydrogel exhibit high optical transparency. As shown in Fig. 2(c), their light transmittance in the visible region is higher than 75% and the image beneath the hydrogel can be clearly seen, which is beneficial for their application in practical wearable devices. Fig. 2(d) shows the Fourier transform-infrared (FTIR) spectra of the DN hydrogel and organohydrogels. The peaks at 1030 cm^{-1} for symmetric C–O stretching with C–O–C, and 1120 cm^{-1} for asymmetric C–O–C stretching, and 1320 cm^{-1} for C–H deformation with secondary alcohols appeared in the FTIR spectra, which was in agreement with the molecule structure of alginate. Furthermore, the FTIR peaks at 1450 cm^{-1} for in-plane $\mathrm{CH_2}$ scissoring and 3200 cm^{-1} for N–H stretching agreed well with the molecule structure of PAM. These results further confirmed the presence of PAM and CA dual networks in the as-prepared hydrogels.[41] Besides, the wide and strong peak in the high wavenumber region ($\sim$3400 cm^{-1}) revealed that there were lots of hydrogen bonds inside both the hydrogel and organohydrogels.

The photographs in Fig. S1 (ESI†) show that this hydrogel can withstand various deformations, such as 0–550% tensile strains, 1400% tensile strains, 45° bending and 360° twisting, confirming the excellent deformability due to the unique DN structure of the hydrogel. Note that about 1400% tensile strain and more than 580 kPa tensile stress were achieved in this hydrogel, which are unprocurable for most existing gas-sensing materials (Fig. 2(e)). The organohydrogels exhibited slightly decreased maximal tensile strains (more than 1100%) compared with the DN hydrogel, but their maximal stresses were larger at the same strain, reflecting the higher mechanical toughness. By extracting the regional slopes of linearly fitted stress–strain curves, the Young's moduli of the pristine hydrogel and organohydrogel obtained by soaking in Gly for 30 and 60 min were determined as 269, 302 and 345 kPa, respectively (Fig. 2(f)). The enhanced toughness after solvent replacement is mainly because Gly molecules are able to form hydrogen bonds with water and polymer molecules, resulting in denser polymer networks. This is the reason why the toughness of the gel increases with prolonged immersion time in Gly.

Although the outstanding mechanical properties (high stretchability and toughness) of DN hydrogels make them promising to be applied in flexible electronics, the inferior stability greatly hinders their long-term stable operation. For our DN tough hydrogel, since the introduced $\mathrm{CaCl_2}$ was able to absorb water molecules from the environment due to its hydration effect, it possessed a better moisture retention capacity compared with ordinary hydrogels, resulting in the increased anti-drying ability. Furthermore, Gly is a common moisturizing and antifreeze ingredient in skincare products and rarely causes harm to the human body.[30,38,40] It is envisaged that the anti-drying and anti-frost capabilities can be further enhanced by soaking the DN hydrogels in Gly to obtain organohydrogels without sacrificing other properties.[39] Herein, the moisture retention ability of the hydrogels and organohydrogels was evaluated by observing their appearance and measuring their weight and resistance variations after being exposed to the environment of 25 °C, and 50% relative

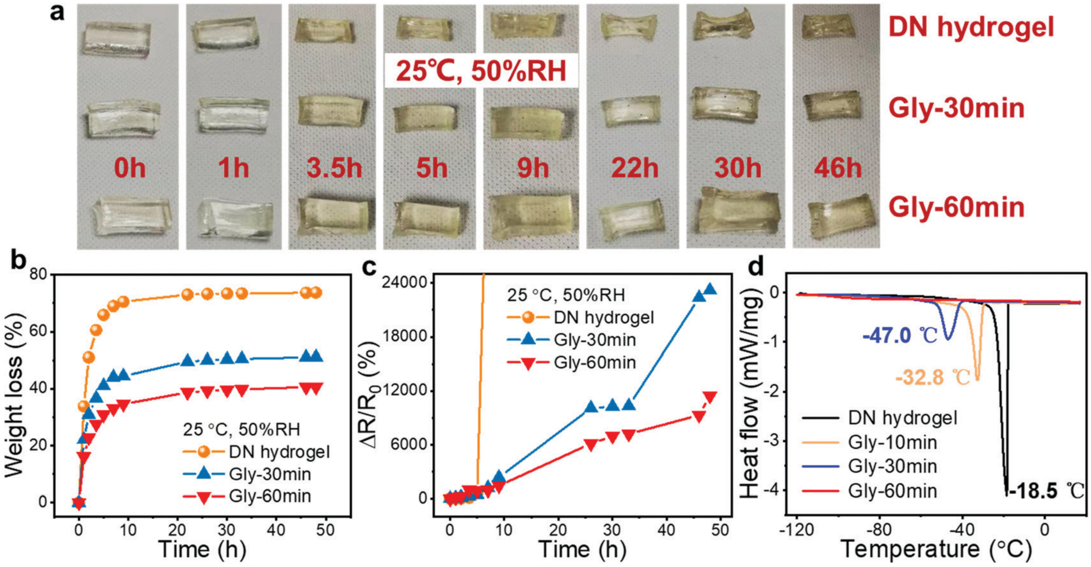

Fig. 3 (a) Optical images showing the morphology evolutions of the pristine hydrogel and organohydrogels obtained by soaking in Gly for 30 and 60 min when stored at 25 °C, 50%RH for a series of time. (b) The relationship between weight loss percentage and time. (c) Curves showing the relative resistance variation *versus* time. (d) DSC spectra indicating the freezing points of the hydrogel and organohydrogels.

humidity (RH) for different periods of time (Fig. 3(a)–(c)). According to the results, the DN hydrogel lost its moisture rapidly as its weight loss reached about 70% after only 5 h of storage. Therefore, the hydrogel shrunk remarkably. Along with this, the conductivity of the hydrogel also deteriorated drastically due to the dehydration. By contrast, the organohydrogels could keep their appearances, weights and electrical conductance for a long time, confirming the moisture retention effect of the introduced $CaCl_2$ and Gly. In this case, the $CaCl_2$ and Gly inside organohydrogel can reduce the vapour pressure and retard the water evaporation process. Also, the Gly molecules can form hydrogen bonds with water molecules inside the hydrogels, further weakening the loss of water and enhancing the moisture retention ability. In addition to the inhibitory effect, the $CaCl_2$ and Gly molecules can even be able to assimilate water molecules from ambient and thus the remarkable anti-drying ability of the organohydrogels can be achieved. By comparing the appearance, weight and resistance variations of two organohydrogels obtained by soaking the hydrogel in Gly for 30 and 60 min, respectively, it is found that the prolonged soaking time in Gly leads to a more significant improvement in the moisture retention ability of the hydrogels, which could be ascribed to the more thorough solvent replacement between water and Gly molecules, leading to the lower content of freezable free water and the higher content of non-freezing bound water.

Except for the moisture retention feature, the incorporation of $CaCl_2$ and Gly also imposes a positive effect on the anti-freezing capacity of the hydrogels. Dynamic scanning calorimetry (DSC) measurement was conducted to evaluate the phase transition temperatures (freezing points) of the DN hydrogels and organohydrogels. As shown in Fig. 3(d), the freezing point of the DN hydrogel is −18.5 °C, which is lower than that of pure water. The slightly boosted anti-freezing capacity can be ascribed to the hydration effect of $CaCl_2$ on the formation of ice crystals. Therefore, the freezing point of DN hydrogels is lower than that of water. By contrast, a better anti-freezing capacity was found in the organohydrogels. As the soaking time was prolonged from 10 to 30 min, the freezing point of the organohydrogel dropped from −32.8 to −47.0 °C. When the soaking time was further extended to 60 min, it is worth noting that the organohydrogel did not exhibit the conspicuous phase transition even though the

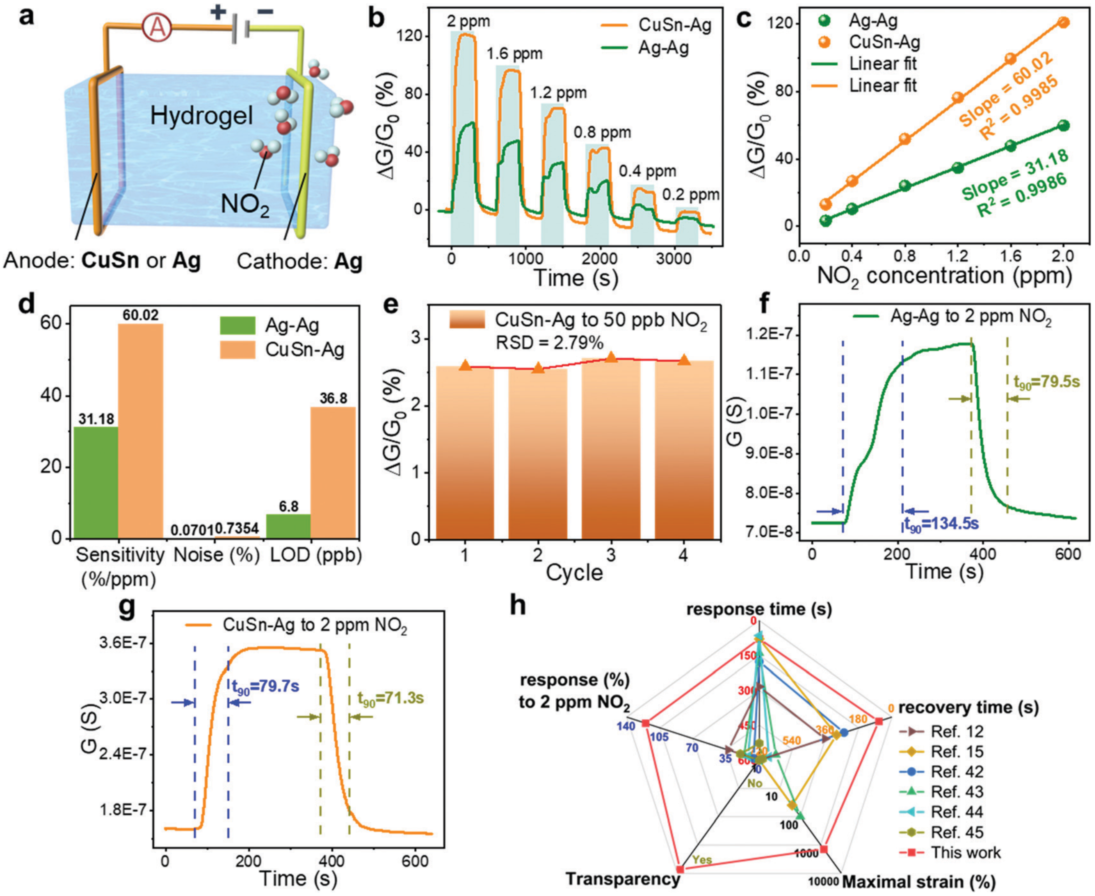

Fig. 4 NO_2 sensing properties of the DN hydrogel-based sensor. (a) Schematic diagram showing the device structure of the hydrogel-based sensor. (b) Dynamic responses curves of the Ag–Ag and CuSn–Ag sensors to a series of NO_2 concentrations. (c) Linearly fitted response *versus* NO_2 concentration, from which the sensitivities were derived. (d) The comparison of the Ag–Ag and CuSn–Ag sensors in terms of the sensitivity, noise and LOD. (e) Repetitive sensing tests of the CuSn–Ag sensor toward 50 ppb NO_2. (f) and (g) Analyses of the response and recovery times of the Ag–Ag and CuSn–Ag sensors to 2 ppm NO_2. (h) The performance comparison of different flexible NO_2 sensors.

temperature was declined to as low as −120 °C, showing the prominent effect of Gly in improving the freezing resistance. Both the hydrogen bonds formed between Gly and water molecules and the strong bonding between Ca^{2+}/Cl^{-} and water molecules reduce the content of free water in the hydrogel and meanwhile increase the content of non-freezing bonded water, which hinders the formation of ice crystals at low temperatures. Furthermore, the hydrogen bonds formed between water molecules can be inhibited, leading to a low freezing point.

2.2 NO_2 sensing performance and mechanism

To establish a hydrogel-based gas sensor, two metal wires were used as electrodes to connect to the two ends of the hydrogel (Fig. 4(a)). During the gas-sensing test, a DC voltage was applied to this sensor and the sensing performance was evaluated by recording the conductance variation of the sensors (Experimental section). To investigate the impact of the electrode material on the NO_2 sensing performance of the hydrogel, two collocations of electrodes were employed: (1) both the anode and cathode were Ag, and (2) the anode and cathode were CuSn alloy and Ag, respectively; and the corresponding fabricated gas sensors were denoted as Ag–Ag and CuSn–Ag sensors, respectively. Before evaluating the gas sensing properties, an appropriate DC voltage should be selected so that NO_2 can be easily detected and is not interfered with by other factors. This is because a too high DC voltage will lead to a high base current, high power consumption and low selectivity in practical applications, while a too low voltage is insufficient to induce the redox reaction at the electrode–hydrogel interface. Therefore, we have executed the gas sensing tests when applying different voltages (0.5, 1 and 1.5 V, respectively). As shown in Fig. S2 (ESI†), when the voltage is 1 V, the current change reaches the maximum. Whereas, at the bias of 1.5 V, NO_2 hardly causes any current change, which may be attributed to the high base current. Thus, we infer that the redox potential of NO_2 is around 1 V with the current sensor configuration. However, the voltage of 1 V will lead to serious electrode consumption due to the high redox reaction rate, so a power supply voltage of 0.5 V is specified for the subsequent NO_2 sensing tests, which is beneficial for acquiring obvious responses with long device lifespan.

As shown in Fig. 4(b), the conductance of both Ag–Ag and CuSn–Ag sensors increased promptly when a NO_2 atmosphere was introduced to the sealed chamber, which meant that the charge flow process in the circuit has been promoted. Herein, the response ($\Delta G/G_0\%$) is defined as the relative change in conductance (ΔG) relative to the initial conductance (G_0) of the sensor. It could be found that the responses of both the two sensors varied with the NO_2 concentration, demonstrating the capability of the sensors to distinguish different NO_2 concentrations. Interestingly, the response of the sensor remarkably increased when the anodic metal (Ag) was replaced with CuSn alloy (Fig. 4(b)). For instance, the Ag–Ag sensor exhibited a relatively good response of 60% to 2 ppm NO_2, while a larger response of 121.1% was observed when the CuSn–Ag sensor was applied to detect NO_2 with the same concentration, which was twice higher than that of the Ag–Ag sensor. As shown in Fig. 4(c), the response of these sensors showed a satisfactory linear relationship with the NO_2 concentration (the values of R^2 are 0.9986 and 0.9985 for Ag–Ag and CuSn–Ag sensors, respectively), and the sensitivity could be obtained from the slope of the linearly fitted response-NO_2 concentration curve. As a result, the sensitivities of the Ag–Ag and CuSn–Ag sensors were derived as 31.18 and 60.02% ppm^{-1}, respectively. Notably, the highly sensitive detection of gases at the ppb level has received widespread attention due to the huge messages that can be transmitted by trace gases in the microenvironment. Attractively, the theoretical limits of detection (LOD) of the Ag–Ag and CuSn–Ag sensors were calculated as 6.8 and 36.8 ppb, respectively, which was preeminent at present and much lower than the annual average exposure limit recommended by the US EPA (53 ppb NO_2) (Fig. S3, Tables S1–S3 and Supporting text, ESI†). As shown in Fig. 4(d), even though the CuSn–Ag sensor exhibited higher sensitivity (60.02% ppm^{-1}) than the Ag–Ag sensor (30.18% ppm^{-1}), its noise (0.7354%) was greater than that of the Ag–Ag sensor (0.0701%). Thus, the Ag–Ag sensor possessed lower LOD.

Fig. 4(e) shows the repetitive response of the CuSn–Ag sensor to NO_2 with the extremely low concentration of 50 ppb for four consecutive cycles. Neither obvious degeneration nor drastic mutation in response was observed in the repeated sensing test toward NO_2 with the same concentration with the small relative standard deviation (RSD) of 2.79%, indicating the satisfactory repeatability, reproducibility and detecting potential at ultralow NO_2 concentration. Although 50 ppb is the lowest NO_2 concentration provided by our current experimental setup, the sensor should be capable of detecting lower NO_2 concentration according to the theoretical LOD. In addition to these sensing characteristics discussed above, the speeds of response and recovery are also very important indicators for evaluating the performance of gas sensors, and it had been investigated in detail here. Fig. 4(f) and (g) display the dynamic response and recovery curves of the Ag–Ag and CuSn–Ag sensors to 2 ppm NO_2, respectively, from which their response and recovery times (t_{90}) were subsequently obtained. Obviously, both the response time (79.7 s) and recovery time (71.3 s) of the CuSn–Ag sensor were less than that of the Ag–Ag sensor (134.5/79.5 s), reflecting faster response/recovery speeds. Note that the signal of the sensors returned to the initial level completely at room temperature without demanding thermal or light activation, reflecting the excellent reversibility.

Fig. 4(h) and Table S4 (ESI†) show the performance comparison of some previously reported flexible NO_2 sensing materials with this ion-conductive hydrogel.[12,15,42–45] Among these, our hydrogel-based NO_2 sensor possessed superior sensing performance regarding the operation temperature, sensitivity, LOD, response and recovery time, *etc.*, better stretchability (more than 1000% strain) and higher optical transmittance. In particular, the room-temperature operation of the hydrogel sensors bypasses the demand of thermal or UV activation as usually utilized in gas sensors based on conventional NO_2 transducing materials to improve the sensitivity and reversibility.

The capability of working in an anaerobic environment also fits for application in some specific anaerobic situations. Notably, most existing NO_2 sensing materials lacks intrinsic stretchability and transparency. Hence, the extremely stretchable and transparent hydrogel-based gas sensors developed in this work show uniqueness and prominent superiority in various aspects, and present great promise in emerging wearable applications.

Different from traditional chemiresistor-type gas sensors based on metal oxide semiconductors, in which the surface adsorption of oxygen and the formation of an electron depletion layer are vital for the generation of a response, here the ion-conducting DN hydrogel functioned as an electrolyte and the gas responsiveness of the sensor was more related to the reactions at the electrode–hydrogel interface. Therefore, these hydrogel gas sensors are capable of operating in the absence of oxygen, whereas the operation of traditional metal oxide-based NO_2 sensors necessitates the presence of oxygen. In an anaerobic nitrogen environment, when a voltage of 0.5 V is applied to the sensor, the current formed is mainly caused by the directional migration of ions inside the hydrogel and the formation of a double electric layer, which belongs to the non-Faraday current. When NO_2 molecules are introduced, oxidation and reduction reactions will occur at the anodic and cathodic electrodes that connected with the hydrogels, respectively, leading to the generation of extra Faraday current and the increment of the current/conductance, as shown in Fig. 1(c). Taking the Ag–Ag sensor as an example, the oxidation reaction occurred at the anode–hydrogel interface (Ag was oxidized to Ag^+), while NO_2 molecules were reduced in the cathode–hydrogel interface, as shown in eqn (1) and (2), respectively. Therefore, the corresponding Faraday current would lead to an increase in the total current, resulting in a clear response. To verify the above proposed sensing mechanism, the NO_2 sensing tests were executed when the anode or cathode of the sensor was closely shielded using a stretchable Ecoflex film. For example, the cathode of the CuSn–Ag sensor was shielded by Ecoflex so that the NO_2 molecules would fail to arrive at the cathode–hydrogel interface, as shown in Fig. 5(a). It can be seen from Fig. 5(b) that the sensor whose anode was shielded still exhibited obvious responses to NO_2, but the sensor whose cathode was shielded failed to respond to NO_2 regardless of the concentration. This phenomenon offers powerful evidence that the reaction of NO_2 molecules occurs in the cathode rather than the anode.

$$\text{Anode: } Ag \rightarrow Ag^+ + e^-, \quad Ag^+ + Cl^- \rightarrow AgCl \tag{1}$$

$$\text{Cathode: } NO_2 + 2e^- + H_2O \rightarrow 2OH^- + NO \tag{2}$$

To further explore the sensing mechanism, both the morphology and composition of the electrodes before and after undergoing the NO_2 sensing test for 6 h were analysed by a scanning electron microscope (SEM) equipped with energy-dispersive spectroscopy (EDS), as shown in Fig. 5(c)–(f) and Fig. S4 and S5 (ESI†). The morphology of the pristine Ag electrode without being subjected to the gas sensing test was flat and homogeneous (Fig. 5(c)). The superficial black spots stemmed from the spontaneous oxidation of Ag in the air before being exploited to serve as the electrode. After undergoing the

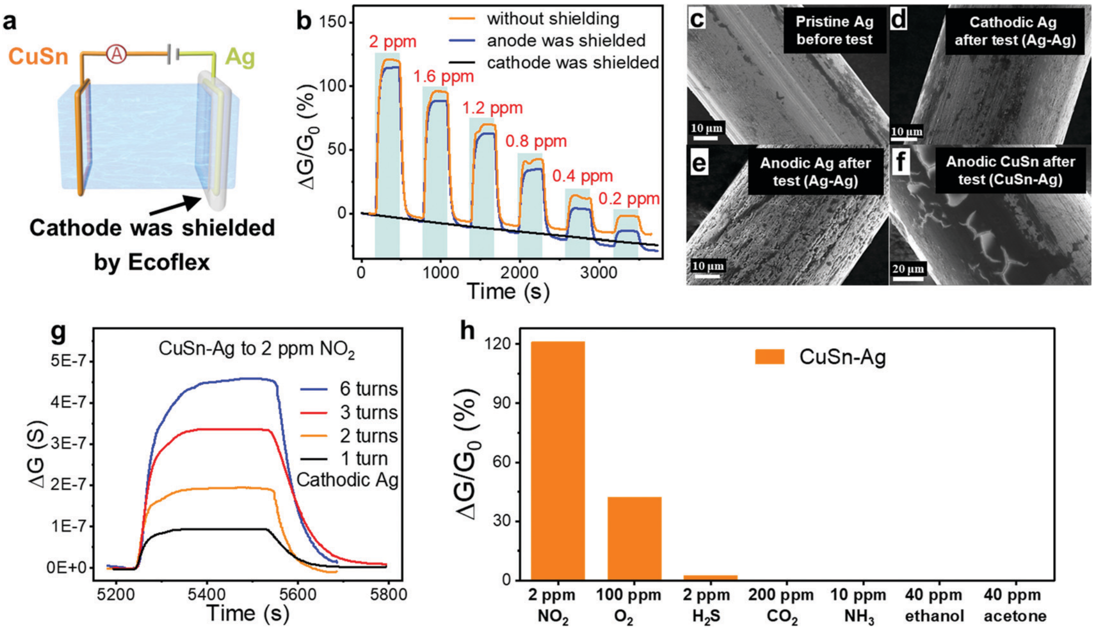

Fig. 5 (a) Schematic diagram showing the cathode of the CuSn–Ag sensor shielded by Ecoflex. (b) Dynamic curves showing the responses of the CuSn sensor to a series of NO_2 concentrations while the anode or cathode was shielded by Ecoflex, or neither was shielded. (c) SEM image of the Ag electrode before the NO_2 sensing test. SEM images of (d) cathodic Ag of the Ag–Ag sensor, (e) anodic Ag of the Ag–Ag sensor and (f) anodic CuSn of the CuSn–Ag sensor after the NO_2 sensing test. (g) Dynamic curves showing the conductance changes of the CuSn–Ag sensor in response to 2 ppm NO_2 when different turns of cathodic Ag wire were applied. (h) Comparison in the responses of the hydrogel-based sensors to various gases, including 2 ppm NO_2, 100 ppm O_2, 2 ppm H_2S, 200 ppm CO_2, 10 ppm NH_3, 40 ppm ethanol, and 40 ppm acetone, respectively.

sensing test, the morphology of the cathodic Ag of the Ag–Ag sensor was similar to that of the pristine Ag electrode (Fig. 5(d)), indicating that the cathode was hardly oxidized or corroded during the gas sensing test. According to eqn (2), the products after cathodic reactions were OH^- inside the hydrogel and gaseous NO. Therefore, the gas sensing process hardly changed the cathodic Ag, while it functioned as the catalyst to promote the redox reactions. In contrast, the morphology of anodic Ag of the Ag–Ag sensor seemed different from the pristine Ag electrode obviously (Fig. 5(e)). Specifically, the morphology of the Ag anode was relatively rough, and a lot of cracks appeared on its surface, which was attributed to the participation of anodic Ag in the reactions as a reactant, as shown in eqn (1). Similarly, as for the CuSn–Ag sensor, the morphology of the cathodic Ag was still maintained after the sensing test (Fig. S5, ESI†), whereas less cracks were observed on the anodic CuSn (Fig. 5(f)), demonstrating the important role of the electrode material in the gas responsive behaviour of the ion-conductive hydrogel in addition to itself. Differently, both the number and density of cracks on the anodic CuSn were much weaker than that of anodic Ag, which could be attributed to the better corrosion resistance of CuSn. On one hand, Cu and Sn were able to form a solid solution, enhancing the corrosion immunity. On the other hand, the oxide layer formed by the oxidation of Sn would further hinder the corrosion of Cu.[46] This demonstrates that the sensing performance of the hydrogel sensors (*e.g.* the lifespan and durability of electrode) can be optimized by programming the electrode materials.

The response variation induced by different anodes should be attributed to the difference in the electrode potentials. Although it is difficult to acquire the exact electrode potentials in our sensor due to the complex composition of both the hydrogel and electrode, standard electrode potentials could provide a reference for analysing the response variation brought by different anodes. As shown in eqn (3)–(6),[47] the Ag^+/Ag electrode possesses a much higher standard electrode potential than the Cu^{2+}/Cu, Cu^+/Cu and Sn^{2+}/Sn electrodes. In other words, Ag^+ exhibits the highest oxidability, and the Ag electrode manifests the lowest reducibility. In the anode, the tendency of Ag to be oxidized is weaker than that of Cu and Sn. According to the conservation of charge, the reduction reaction in the anode also promotes the oxidation reaction in the cathode. Therefore, the reduction reaction (eqn (2)) of CuSn–Ag electrodes in the cathode is stronger than that of Ag–Ag electrodes, leading to the higher sensitivity of the CuSn–Ag sensor. To obtain higher sensitivity, employing electrodes with lower standard electrode potentials could be an effective method. These experimental results also collectively consolidated the aforementioned gas sensing mechanism. Based on the redox reactions that occurred at the electrode–hydrogel interface, it is supposed that the interfacial contact area should affect the gas sensing properties. To verify this, the gas sensing response of CuSn–Ag sensors with different turns of cathodic Ag was measured and compared (Fig. 5(g)). As the turns of cathodic Ag increased, larger conductance changes were observed. This is because the larger contact area of the cathode with the hydrogel is able to provide more reaction sites and thus enables more evident responses, making the gas sensing properties facilely programmable.[47]

$$Ag^+ + e^- = Ag, \quad E = 0.80\ V \tag{3}$$

$$Cu^+ + e^- = Cu, \quad E = 0.52\ V \tag{4}$$

$$Cu^{2+} + 2e^- = Cu, \quad E = 0.34\ V \tag{5}$$

$$Sn^{2+} + 2e^- = Sn, \quad E = -0.13\ V \tag{6}$$

Lots of gases such as CO_2 and NH_3 might interfere with the NO_2 sensing, necessitating the investigation of the selectivity. Fig. 5(h) and Fig. S6 (ESI†) show the responses of the CuSn–Ag sensor to various gases, including NO_2, O_2, H_2S, CO_2, NH_3, ethanol and acetone. Considering that oxygen (O_2) is a common oxidizing gas in daily life, we have also executed a sensing test to 100 ppm O_2. The O_2 concentration is 50 times higher than that of 2 ppm NO_2. It can be seen that the CuSn–Ag sensor exhibits a response of about 42% to 100 ppm O_2, which is one-third that of 2 ppm NO_2 (121.1%). Furthermore, our sensor is capable of detecting NO_2 in the presence of 21% O_2 (with air background) (Fig. S7, ESI†), reflecting the capability of the NO_2 sensor to work under both aerobic and anaerobic conditions, which is a unique advantage in comparison with traditional metal oxide semiconductor based NO_2 sensors. It's possible to optimize the supply voltage and modify the electrode material to preclude the interference of oxygen in NO_2 sensing.[48]

It could be seen that this sensor hardly responded to gases except for NO_2 and O_2, indicating the excellent selectivity. According to the sensing mechanism mentioned above, the requirement of obtaining a high response is that the target gas can be reduced in the cathode. NO_2 molecules were able to be reduced to NO in the cathode and promote the charge transfer process. By contrast, the other interfering gases were not easily reduced in the cathode, failing to promote the charge transfer process in the circuit and leading to low responses. Consequently, the outstanding selectivity of this NO_2 sensor was achieved here.

Although the incorporation of Gly in the hydrogel enhanced the moisture retention capacity, its water content and electrical properties would change as well, inevitably leading to the variations in gas sensing performances. As shown in Fig. 6(a), compared with the CuSn–Ag DN hydrogel sensor, the corresponding organohydrogel sensor exhibited a decreased responses to NO_2, and the sensitivity declined from 60.02 to 46.28% ppm^{-1} accordingly (Fig. 6(b)). During the soaking process, Gly molecules could diffuse into the hydrogel under the concentration gradient and replace part of the free water molecules to achieve the Gly–water binary solvent system. As water participates in the redox reactions as a reactant (eqn (2)), the declined water content would result in the attenuated cathode reaction, thereby decreasing the sensitivity in NO_2 detection. In addition, the hydrogen bonds between Gly and water molecules may fetter the water molecules inside the hydrogel, hindering the cathodic reaction. However, the incorporation of Gly into the hydrogel enhances the stability of the gas sensor. After exposure to ambient air for 20 days, it could be seen from

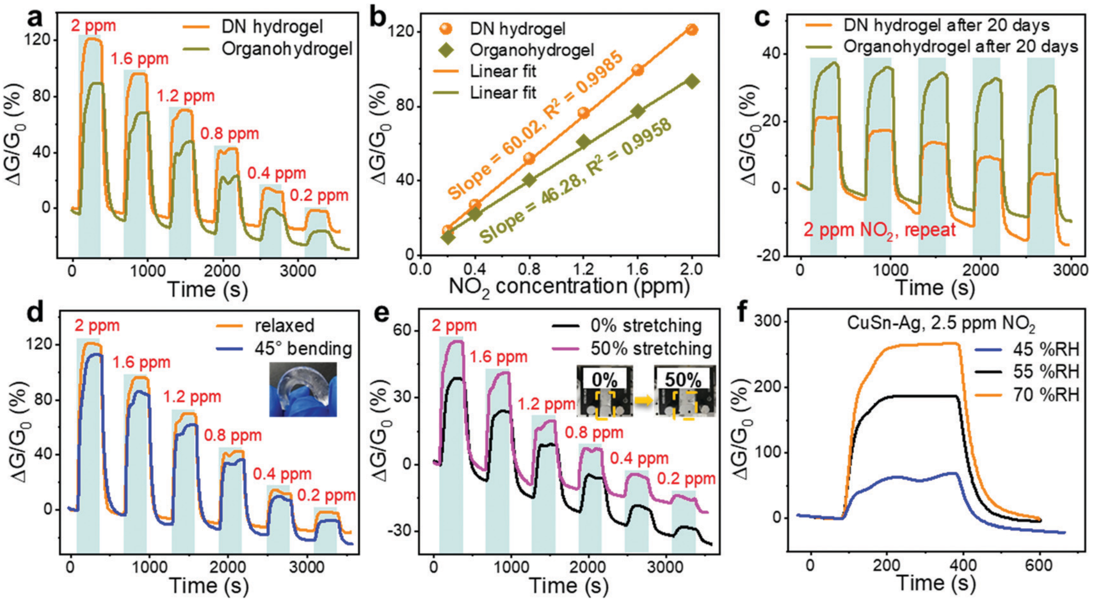

Fig. 6 (a) Dynamic responses to a series of NO_2 concentrations for the DN hydrogel and organohydrogel-based sensors with CuSn–Ag electrodes. (b) Linear fitting response *versus* NO_2 concentration curves illustrating the sensitivities (slope) of the hydrogel and organohydrogel-based sensors. (c) Dynamic and repeated responses of the two kinds of sensors to 2 ppm NO_2 after exposure to ambient air for 20 days. (d) Dynamic responses of the hydrogel-based sensor to 0.2–2 ppm NO_2 in relaxed and 45° bending states. (e) Dynamic responses of the hydrogel-based sensor to 0.2–2 ppm NO_2 at 0% and 50% stretching strains. (f) Time-dependent responses of the hydrogel-based sensor to 2.5 ppm NO_2 under different relative humidities.

Fig. 6(c) that both the DN hydrogel and organohydrogel sensors still exhibited clear responses to NO_2 although the response deteriorated. However, the newly fabricated DN hydrogel sensor showed higher and lower responses to 2 ppm NO_2 than the organohydrogel sensor before and after exposure for 20 days, respectively, indicating the better long-term stability of the organohydrogel sensor. This could be attributed to the much better moisture retention ability of the organohydrogel as mentioned earlier. The conductivity of the organohydrogels could be maintained for a long time, but the DN hydrogel lost moisture rapidly, leading to the degraded conductivity. Thus, the organohydrogel sensor possessed superior stability and was more appropriate for long-term applications.

Hydrogel-based gas sensors are considered to have great potential to be applied as wearable electronic devices due to their excellent deformability, which is advantageous over traditional rigid gas sensors. As such, we have also evaluated the NO_2 sensing performances of the hydrogel-based sensor under different deformation states such as tensile and bending strains. Although several deformations were applied to the hydrogels, the electrical conductivity did not forfeit (Fig. S8, ESI†). As shown in Fig. 6(d), the bending deformation showed a negligible effect on the electrical properties, electrode–hydrogel interface, and internal composition of the DN hydrogel, such that the sensor under bending deformation exhibited similar sensing behaviours to that in the relaxed state. In order to carry out the gas sensing test under tensile deformation, the hydrogel sensor is usually stretched in advance and then fixed on the glass substrate so that the tensile strain is maintained during the test. However, this will cause one side of the electrode–hydrogel interface to be shielded by the substrates, leading to the decreased interfacial surface area exposed to gas and the declined response. Therefore, an unstretched hydrogel sensor (0% strain) was also fixed on the substrate for comparison. As shown in Fig. 6(e), the sensor under 50% stretching strain exhibited an enhanced response compared to that without stretching. When the hydrogel was stretched, its initial conductance (G_0) would be reduced due to the geometric effect, so the identical electrode reactions (ΔG) caused higher responses ($\Delta G/G_0$). This manifests that the gas sensing performance of the hydrogel-based sensor can be facilely and mechanically tuned by applying appropriate tensile strain.

In addition to mechanical deformations, hydrogel-based sensors are expected to have the capability to operate even though the environmental humidity changes. Nevertheless, humidity is a common factor that influences the room-temperature sensing performance of gas sensors. Therefore, the impact of environmental humidity on the NO_2 sensing characteristics of the hydrogel sensor was also investigated. As shown in Fig. 6(f), the responses of the CuSn–Ag sensor would increase remarkably as the RH elevated, suggesting an interesting humidity activation effect. Specifically, the response augmented from 68.31% to 267.05% when the RH increased from 45% to 70%. This is because the moist circumstance is able to provide abundant water molecules to facilitate the electrochemical reactions so that the electrode reaction can be executed promptly and thoroughly (eqn (2)), resulting in enhanced sensitivity. This demonstrates the capability of the hydrogel-based sensors to work under different humidities with an unimpaired response with increased humidity level.

Notably, the stretchable DN hydrogel sensor also displays a prominent electromechanical response. Fig. S9 (ESI†) shows the electromechanical properties of the hydrogel sensor, which can be employed to enrich the functionality of this device. On the one hand, the tensile strain may interfere with the gas sensing performance in wearable applications. To preclude the interference of tensile strain and obtain accurate gas information, calibrating this sensor by deducting the electromechanical response is an appropriate method. On the other hand, integrating the gas-sensing and strain-sensing modules to achieve multi-functional sensors is also promising for practical wearable applications. The resistance of the sensor increased immediately when different tensile strains were applied, which was attributed to the geometric effect, that was the simultaneous elongation and the narrowing of the ion-conducting channel upon stretching. It is worth noticing that the gauge factor in strain sensing is as high as 5.05, reflecting the high sensitivity. Furthermore, a broad detection range (5–600% strain) and excellent repeatability are displayed by the hydrogel-based sensor, suggesting the high strain sensing performance as well.

2.3 Real-time alarm demonstration

To express the practical application of the hydrogel-based NO_2 sensor, we also executed alarm demonstrations by virtue of two ways: (1) light and buzzer alarms on a circuit board (Demo-1) and (2) a wireless alarm *via* an applet in a smartphone (Demo-2). The whole demonstration system contains three sections: sensor, hardware and software systems, which are minutely illustrated in Fig. 7(a) and (b) and the ESI.† In Demo-1 (Fig. 7(c)–(f) and Supporting Movie 1, ESI†), the signal of the sensor is transmitted to the circuit board for processing in real time. The current would increase if the NO_2 concentration increases in the atmosphere. When the response current reached the preestablished threshold, the light and buzzer on the circuit would turn to the ''on'' state to alarm, which warns people to be careful of NO_2 with dangerous concentrations. As shown in Fig. 7(c), the alarm system kept the ''Normal'' state since the current was lower than the threshold. It would turn to the ''Alarm'' state if the real-time current reached the threshold and the light and buzzer would switch on simultaneously to give timely warning (Fig. 7(d)). After turning off the NO_2, the current would decrease, and the alarm system would change from the ''Alarm'' state to ''Normal state'' again (Fig. 7(e) and (f)).

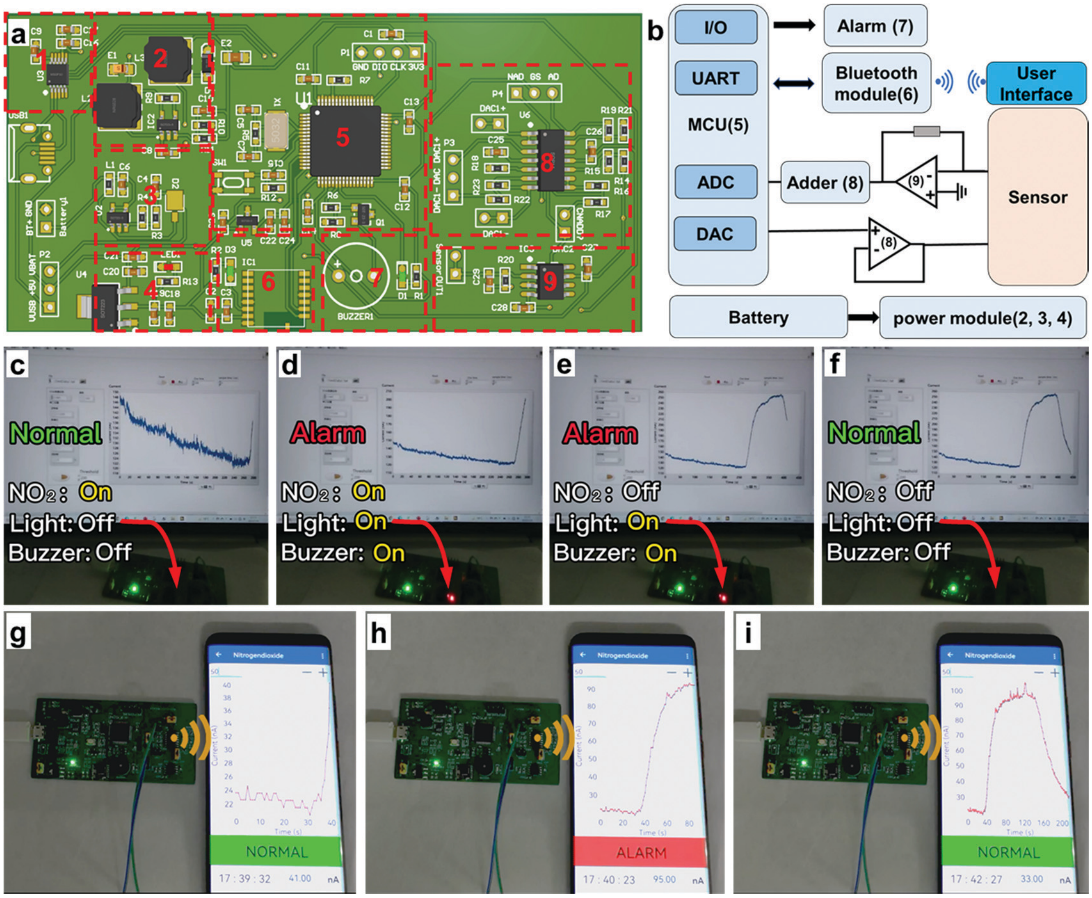

Fig. 7 (a) The photograph of the circuit board that is adopted to process data from the hydrogel-based NO_2 sensor. (b) A schematic representing the structure and function of the alarm system. The alarm demonstration by light and buzzer: (c) the hydrogel-based NO_2 sensor was exposed to 2 ppm NO_2 atmosphere and the current began to rise. (d) The current reached the threshold and the system turned to the ''Alarm'' state, as both the light and buzzer were ''on''. (e) The NO_2 atmosphere was evacuated and the current began to decline. (f) The current decreased to below the threshold and the system turned to the ''Normal'' state, as both the light and buzzer were ''off''. The wireless alarm demonstration by an applet in a smartphone: (g) The current began to rise since NO_2 molecules were introduced. (h) The current reached the threshold and the applet turned to the ''Alarm'' state. (i) The current declined since NO_2 atmosphere was evacuated and the applet turned to the ''Normal'' state again.

In addition to the aforementioned light and buzzer alarms, we also executed a user-friendly wireless alarm by designing an applet in a smartphone. In Demo-2 (Fig. 7(g)–(i) and Supporting Movie 2, ESI†), the circuit board received and processed the signal from the hydrogel-based NO_2 sensor, which was similar to Demo-1. Differently, the real-time data that have been processed were wirelessly transferred to the smartphone and displayed by an applet. Users could see the values of real-time current and corresponding NO_2 concentration conveniently. If the current reached the threshold, the applet would turn to ''Alarm'' mode, giving an early warning to the users to take precautions. This demonstration provides inspiration and evidence that a hydrogel-based NO_2 sensor could be applied in advanced portable electronics and IoT technology for practical applications.

3. Conclusion

In summary, highly stretchable, sensitive, selective, and transparent hydrogel-based NO_2 sensors have been fabricated successfully by employing an ion-conductive and tough DN hydrogel/organohydrogel as a novel transducing material. The sensor exhibited a high sensitivity (60.02% ppm^{-1}), low LOD (6.8 ppb), impressive selectivity, reversibility and linearity to NO_2 at room temperature. A specially designed electrode shielding experiment combined with the microscopic analyses validated that the electrochemical reactions occurring in the electrode–hydrogel interfaces resulted in the increased conductance of the device and an evident response to NO_2. When the sensor was exposed to a NO_2 atmosphere, the anodic metal tended to be oxidized and NO_2 molecules tended to be reduced in the cathode, accounting for the sensing mechanism of the ion-conducting hydrogels. Based on this mechanism, it was found that the sensing performance could be enhanced when Ag–Ag electrodes were replaced by CuSn–Ag electrodes, revealing the significant role of the electrodes in the gas responsiveness of ion-conducting hydrogels. Since it is not necessary for oxygen to participate in the redox reactions, the sensors are able to work in an anaerobic environment, which is generally not accessible for traditional metal oxide gas sensors.

Neither large mechanical deformations nor enlarged interfacial surface area degraded the sensing performance, but rather enhanced the response, providing creative pathways to optimize the sensing performance and fit for wearable application. The introduction of Gly into the hydrogel not only endowed excellent moisture-retention and anti-freezing capacities and toughness, but also maintained the gas-sensing performance for a long term. Furthermore, the signal from the sensor was processed by a lab-made circuit and used for real-time sound/light alarms and a wireless applet alarm when the NO_2 concentration exceeds the threshold, presenting great potential for practical applications. This work provides in-depth insights into the performance enhancement, mechanism and application of hydrogel-based stretchable gas sensors, which inspires the development of various deformable, high-performance, and room-temperature gas sensors using ion-conducting hydrogels/organohydrogels as a family of novel sensing materials.

4. Experimental section

Preparation of DN hydrogels and organohydrogels

The PAM/CA hydrogel was prepared in two steps, which was different from the previously reported one-pot method (Fig. 2(a)).[41,49] It is indispensable to introduce Ca^{2+} into the hydrogel so that sodium alginate (SA) chains can transform into the CA network (Fig. 2(b)). Nevertheless, calcium sulphate ($CaSO_4$) is difficult to diffuse into the hydrogel system due to its low solubility. In addition, SA will transform into CA rapidly if $CaCl_2$ is directly added into the hydrogel precursor, making the gelation process difficult to control. Thus, a two-step synthesis method was proposed to ensure the simple and controllable synthesis of the PAM/CA DN hydrogel. Specifically, acrylamide (AM), sodium alginate (SA), *N*,*N*-methylene bisacrylamide (MBA) and ammonium persulphate (APs) were added into deionized water with the weight ratios of 8 : 1 : 0.005 : 0.05 in the first step. The mixture (with the total weight of 50 g) was stirred at 600 rpm for 30 min to attain complete dissolution. To accelerate the gelling process, 20 μL *N*,*N*,*N*′,*N*′-tetramethylethylenediamine was added into the solution to function as an accelerator. Afterward, the obtained solution was poured into a plastic dish and subsequently kept in a 65 °C oven for 2 h. The AM would crosslink into the first PAM network under the function of a crosslinker, initiator and heat. Secondly, the obtained hydrogel precursor was cut into pieces, which were soaked into the 1 mol L^{-1} $CaCl_2$ solution for 3 h at 25 °C. Ca^{2+} would diffuse into the hydrogel network under the concentration gradient. SA molecules formed the ionic cross-linked network under the function of Ca^{2+} (second network). Subsequently, the obtained DN hydrogel pieces were wiped carefully by tissues. To obtain the organohydrogels, the DN hydrogel pieces were soaked into 6 mL Gly for 1 h to achieve solvent replacement for the preparation of organohydrogels with a Gly–water binary solvent.

Material characterization

The transmittance spectra were obtained using a UV-visible spectrophotometer (Thermo Fisher, Inc. Evolution 220). The FTIR spectra were acquired by a Fourier transform infrared spectroscopy-infrared microscope combined instrument (Thermo Fisher, NICOLET 6700). The DSC results were acquired using a differential scanning calorimeter (Netzsch, DSC-204). The SEM images and EDS results were obtained using a field emission scanning electron microscope (Wavetest, SUPRA 60). When testing the mechanical characteristics (stress–strain curves) of the hydrogels by a tensile testing machine (Wavetest, Instron 5943), we employed strip samples with the size of 40 × 4 × 1.2 mm to guarantee that the samples were clamped tightly.

Fabrication of hydrogel-based sensors

Two metal wires were tied at the ends of a hydrogel piece with a size of 30 × 8 × 6 mm, which served as electrodes. The collocation of electrodes included two types: Ag–Ag and CuSn–Ag. The diameters of the CuSn and Ag wires were 100 and 60 μm, respectively. The distances between the electrodes were set as 15 and 20 mm during all the strain and gas sensing tests, respectively.

Gas-sensing measurement

The sensors were placed in a sealed chamber for measuring the gas sensing properties at room temperature (25 °C) and 60%RH unless otherwise noted. An electrochemical workstation (CH Instruments, CHI760E) was connected with the electrodes of this sensor for monitoring the conductance variation after applying the DC voltage of 0.5 V. The electrical parameters would change when the target gas (NO_2) was introduced into the chamber. Pure nitrogen (N_2) was employed to dilute the 10 ppm NO_2 (balanced by N_2) into various concentrations (*e.g.* 50 ppb to 5 ppm) so that the intrinsic response of the sensor to NO_2 could be obtained. Before and after feeding NO_2 into the chamber, the chamber was purged by N_2. Before NO_2 sensing, the sensors were connected with a 0.5 V power source for 1 h, enabling the conductance of the sensor to reach the stable status. The time and the total flows of every response and recovery step were abidingly set as 300 s and 500 sccm, respectively.

Conflicts of interest

The authors declare no conflict of interest.

Acknowledgements

J. W. acknowledges financial support from the National Natural Science Foundation of China (61801525), the Guangdong Basic and Applied Basic Research Foundation (2020A1515010693), Fundamental Research Funds for the Central Universities, Sun Yat-sen University (22lgqb17), and the Science and Technology Program of Guangzhou (201904010456).

References

1 H.-R. Lee, C.-C. Kim and J.-Y. Sun, *Adv. Mater.*, 2018, **30**, 1704403.

2 Q. Peng, J. Chen, T. Wang, X. Peng, J. Liu, X. Wang, J. Wang and H. Zeng, *InfoMat*, 2020, **2**, 843–865.

3 Q. Ding, Z. Wu, K. Tao, Y. Wei, W. Wang, B.-R. Yang, X. Xie and J. Wu, *Mater. Horiz.*, 2022, DOI: **10.1039/D1MH01871J**.

4 F. Pinelli, L. Magagnin and F. Rossi, *Mater. Today Chem.*, 2020, **17**, 100317.

5 Z. Wu, H. Ding, K. Tao, Y. Wei, X. Gui, W. Shi, X. Xie and J. Wu, *ACS Appl. Mater. Interfaces*, 2021, **13**, 21854–21864.

6 J. Wu, Z. Wu, H. Ding, Y. Wei, W. Huang, X. Yang, Z. Li, L. Qiu and X. Wang, *Sens. Actuators, B*, 2020, **305**, 127445.

7 Z. Yuan, Q. Zhao, C. Xie, J. Liang, X. Duan, Z. Duan, S. Li, Y. Jiang and H. Tai, *Sens. Actuators, B*, 2022, **355**, 131300.

8 R. Kumar, X. Liu, J. Zhang and M. Kumar, *Nano-Micro Lett.*, 2020, **12**, 164.

9 S. W. Lee, W. Lee, Y. Hong, G. Lee and D. S. Yoon, *Sens. Actuators, B*, 2018, **255**, 1788–1804.

10 Y. Xu, L. Zheng, C. Yang, X. Liu and J. Zhang, *Sens. Actuators, B*, 2020, **304**, 127237.

11 Y. Zhang, Y. Jiang, Z. Duan, Q. Huang, Y. Wu, B. Liu, Q. Zhao, S. Wang, Z. Yuan and H. Tai, *Sens. Actuators, B*, 2021, **344**, 130150.

12 J. Wu, Y. Wei, H. Ding, Z. Wu, X. Yang, Z. Li, W. Huang, X. Xie, K. Tao and X. Wang, *ACS Appl. Mater. Interfaces*, 2020, **12**, 20623–20632.

13 P. Yu, X. Li, H. Li, Y. Fan, J. Cao, H. Wang, Z. Guo, X. Zhao, Z. Wang and G. Zhu, *ACS Appl. Mater. Interfaces*, 2021, **13**, 24062–24069.

14 S. B. Kulkarni, Y. H. Navale, S. T. Navale, F. J. Stadler, N. S. Ramgir and V. B. Patil, *Sens. Actuators, B*, 2019, **288**, 279–288.

15 M. A. Islam, H. Li, S. Moon, S. S. Han, H.-S. Chung, J. Ma, C. Yoo, T.-J. Ko, K. H. Oh, Y. Jung and Y. Jung, *ACS Appl. Mater. Interfaces*, 2020, **12**, 53174–53183.

16 Z. Qin, X. Sun, H. Zhang, Q. Yu, X. Wang, S. He, F. Yao and J. Li, *J. Mater. Chem. A*, 2020, **8**, 4447–4456.

17 C.-C. Kim, H.-H. Lee, H. Oh Kyu and J.-Y. Sun, *Science*, 2016, **353**, 682–687.

18 C. Yang and Z. Suo, *Nat. Rev. Mater.*, 2018, **3**, 125–142.

19 X. Lu, Y. Si, S. Zhang, J. Yu and B. Ding, *Adv. Funct. Mater.*, 2021, **31**, 2103117.

20 L. Han, X. Lu, M. Wang, D. Gan, W. Deng, K. Wang, L. Fang, K. Liu, C. W. Chan, Y. Tang, L.-T. Weng and H. Yuan, *Small*, 2017, **13**, 1601916.

21 F. Tao, L. Qin, Z. Wang and Q. Pan, *ACS Appl. Mater. Interfaces*, 2017, **9**, 15541–15548.

22 Y. Wang, F. Chen, Z. Liu, Z. Tang, Q. Yang, Y. Zhao, S. Du, Q. Chen and C. Zhi, *Angew. Chem., Int. Ed.*, 2019, **58**, 15707–15711.

23 B. Yang and W. Yuan, *ACS Appl. Mater. Interfaces*, 2019, **11**, 16765–16775.

24 Z. Wu, L. Rong, J. Yang, Y. Wei, K. Tao, Y. Zhou, B. Yang, X. Xie and J. Wu, *Small*, 2021, **17**(52), 2104997.

25 H. Zhang, W. Niu and S. Zhang, *ACS Appl. Mater. Interfaces*, 2019, **11**, 24639–24647.

26 J. Y. C. Lim, S. S. Goh and X. J. Loh, *ACS Mater. Lett.*, 2020, **2**, 918–950.

27 G. Ge, Y. Lu, X. Qu, W. Zhao, Y. Ren, W. Wang, Q. Wang, W. Huang and X. Dong, *ACS Nano*, 2020, **14**, 218–228.

28 J. Wu, Z. Wu, H. Xu, Q. Wu, C. Liu, B.-R. Yang, X. Gui, X. Xie, K. Tao, Y. Shen, J. Miao and L. K. Norford, *Mater. Horiz.*, 2019, **6**, 595–603.

29 G. Ge, Y. Zhang, J. Shao, W. Wang, W. Si, W. Huang and X. Dong, *Adv. Funct. Mater.*, 2018, **28**, 1802576.

30 H. Sun, Y. Zhao, S. Jiao, C. Wang, Y. Jia, K. Dai, G. Zheng, C. Liu, P. Wan and C. Shen, *Adv. Funct. Mater.*, 2021, **31**, 2101696.

31 F. Mo, Y. Huang, Q. Li, Z. Wang, R. Jiang, W. Gai and C. Zhi, *Adv. Funct. Mater.*, 2021, **31**, 2010830.

32 Y. Dong, E. M. Akinoglu, H. Zhang, F. Maasoumi, J. Zhou and P. Mulvaney, *Adv. Funct. Mater.*, 2019, **29**, 1904290.

33 H. Ding, Z. Wu, H. Wang, Z. Zhou, Y. Wei, K. Tao, X. Xie and J. Wu, *Mater. Horiz.*, 2022, DOI: 10.1039/D2MH00281G.

34 J. Wu, Z. Wu, S. Han, B. R. Yang, X. Gui, K. Tao, C. Liu, J. Miao and L. K. Norford, *ACS Appl. Mater. Interfaces*, 2019, **11**, 2364–2373.

35 J. Wu, Z. Wu, W. Huang, X. Yang, Y. Liang, K. Tao, B.-R. Yang, W. Shi and X. Xie, *ACS Appl. Mater. Interfaces*, 2020, **12**, 52070–52081.

36 H. Zhi, J. Gao and L. Feng, *ACS Sens.*, 2020, **5**, 772–780.

37 L. Liu, T. Fei, X. Guan, H. Zhao and T. Zhang, *Biosens. Bioelectron.*, 2021, **191**, 113459.

38 Y. Jian, B. Wu, X. Le, Y. Liang, Y. Zhang, D. Zhang, L. Zhang, W. Lu, J. Zhang and T. Chen, *Research*, 2019, **2019**, 2384347.

39 F. Chen, D. Zhou, J. Wang, T. Li, X. Zhou, T. Gan, S. Handschuh-Wang and X. Zhou, *Angew. Chem., Int. Ed.*, 2018, **57**, 6568–6571.

40 J. Wu, Z. Wu, Y. Wei, H. Ding, W. Huang, X. Gui, W. Shi, Y. Shen, K. Tao and X. Xie, *ACS Appl. Mater. Interfaces*, 2020, **12**, 19069–19079.

41 J. Y. Sun, X. Zhao, W. R. Illeperuma, O. Chaudhuri, K. H. Oh, D. J. Mooney, J. J. Vlassak and Z. Suo, *Nature*, 2012, **489**, 133–136.

42 J. Wu, Z. Wu, H. Ding, Y. Wei, W. Huang, X. Yang, Z. Li, L. Qiu and X. Wang, *ACS Appl. Mater. Interfaces*, 2020, **12**, 2634–2643.

43 W. Li, R. Chen, W. Qi, L. Cai, Y. Sun, M. Sun, C. Li, X. Yang, L. Xiang, D. Xie and T. Ren, *ACS Sens.*, 2019, **4**, 2809–2818.

44 B. Liu, X. Liu, Z. Yuan, Y. Jiang, Y. Su, J. Ma and H. Tai, *Sens. Actuators, B*, 2019, **295**, 86–92.

45 J.-Y. Kang, W.-T. Koo, J.-S. Jang, D.-H. Kim, Y. J. Jeong, R. Kim, J. Ahn, S.-J. Choi and I.-D. Kim, *Sens. Actuators, B*, 2021, **331**, 129371.

46 I. Mabille, A. Bertrand, E. M. M. Sutter and C. Fiaud, *Corros. Sci.*, 2003, **45**, 855–866.

47 chemeurope.com, Standard electrode potential, https://www.chemeurope.com/en/encyclopedia/Standard_electrode_potential_%28data_page%29.html, (accessed 2021-9-10, 2021).

48 Y. Liang, Z. Wu, Y. Wei, Q. Ding, M. Zilberman, K. Tao, X. Xie and J. Wu, *Nano-Micro Lett.*, 2022, **14**, 52.

49 J. Wang, J. Wei, S. Su, J. Qiu and S. Wang, *J. Mater. Sci.*, 2015, **50**, 5458–5465.